Check for updates

On the epitaxial growth in ALD Co$_3$O$_4$- and NiO-based bilayers†

Renée T. M. van Limpt, [ID] *[a] Cristian A. A. van Helvoirt,[a] Mariadriana Creatore [ID] [a,b] and Marcel A. Verheijen*[a,c]

NiO and Co$_3$O$_4$ are versatile materials studied for a plethora of applications, yet their performance for a specific application relies on the control of their crystallographic texture and corresponding surface facets. Achieving such control can be challenging, often requiring hetero-epitaxial growth on single-crystalline substrates, which are frequently incompatible with the requirements of the application. The combination of NiO and Co$_3$O$_4$ in heterostructures provides potential to control texture due to their similar crystal structures, whilst retaining the possibility to work with more versatile substrates. In this study, atomic layer deposited (ALD) thin films based on cyclopentadienyl precursors and an oxygen plasma are adopted to tailor the crystallographic texture of NiO from ⟨100⟩ to ⟨111⟩ using an ALD Co$_3$O$_4$ template layer, and similarly, to modify the Co$_3$O$_4$ texture from ⟨111⟩ to ⟨100⟩ on a NiO template. The films are shown to conform to the crystal orientation of the template material, whilst crystallizing directly in their own stable crystal structure with corresponding metal atom coordination. Further investigation includes ALD process parameters for NiO growth: the film texture is found to depend on the choice of co-reactant and the above-highlighted hetero-epitaxial relationship is stronger for plasma-based processes. In conclusion, these results demonstrate an original approach for application-oriented crystallographic engineering in thin films.

[a]Eindhoven University of Technology, 5600 MB Eindhoven, The Netherlands.
E-mail: r.t.m.v.limpt@tue.nl, m.a.verheijen@tue.nl
[b]Eindhoven Institute of Renewable Energy Systems (EIRES), 5600 MB Eindhoven, The Netherlands
[c]Eurofins Materials Science Netherlands, 5656 AE Eindhoven, The Netherlands

†Electronic supplementary information (ESI) available: Additional crystallographic information and STEM, XPS and XRD measurements of various Co$_3$O$_4$ and NiO bilayers. See DOI: https://doi.org/10.1039/d5nr01212k

The chemistries of nickel oxide (NiO) and cobalt oxide (Co$_3$O$_4$) are versatile and widely studied for their implementation in various applications such as solar cells,[1–3] supercapacitors,[4–10] gas sensors,[11–14] batteries,[15–22] and (electro-)catalysis.[23–29] A key property influencing the performance of these materials for a specific application is the orientation of the crystals within the film and the type of surface facet correlated to it.[30–37] The NiO (111) facet is, for example, preferred for gas sensors,[38] whilst NiO (110) is more efficient for ethane activation.[39] Similarly, Co$_3$O$_4$ (111) is preferred for Li–O$_2$ batteries,[31,40] whilst the (110) surface is preferred for photothermal methanol oxidation.[41] In the context of oxygen evolution reaction (OER) electrocatalysts in water electrolysis, the optimal facets are Co$_3$O$_4$ (100) and NiO (110). Co$_3$O$_4$ (100) exhibits higher activity due to the formation of a thicker active (oxy)hydroxide skin layer as compared to Co$_3$O$_4$ (111), possibly

due to differences in metal coordination and/or defects.[42–44] Likewise, NiO (110) facets show superior activity by stabilizing the β-Ni(OH)$_2$ form, as opposed to the less active α-Ni(OH)$_2$ form.[45]

Controlling the crystallographic texture of a NiO or Co$_3$O$_4$ film is challenging. Films often lack a preferred growth orientation when deposited on amorphous substrates,[46–60] necessitating hetero-epitaxial growth on crystalline substrates such as c-Al$_2$O$_3$ (0001)[61–66] or MgO (100)[57,63,64,67] to achieve oriented growth.[55,64,68–70] However, these substrates are often not compatible with the targeted applications.

The cubic crystal structures of NiO and Co$_3$O$_4$ differ in the coordination number of their metal atoms. Interestingly, the interplanar distances in several directions of the two crystal lattices are quite compatible; the Co$_3$O$_4$ lattice has ∼4% smaller interplanar distances compared to equivalent spacings in NiO with similar atomic positions of metal atoms.[71,72] This close alignment enables hetero-epitaxy,[73] providing an opportunity to obtain preferred growth orientations for Co$_3$O$_4$ and NiO that cannot be obtained by growing single layers, but may be realized by continuing the texture from the underlying layer.

By combining NiO and Co$_3$O$_4$ in heterostructures, composites and core–shell structures have already been shown to synergistically modulate their chemical and electronic band structures, benefiting applications such as gas sensors, bat-

teries, and electrocatalysis, among others.[73–80] Zhang et al.[73] demonstrated that the NiO–Co_3O_4 interface is metallic, significantly enhancing conductivity and charge transfer during the OER as compared to NiO and Co_3O_4. This heterointerface was therefore identified as the primary driver for improved performance as an OER catalyst. These results suggest that NiO and Co_3O_4 film stacks could also possibly improve performance in various applications. In the context of electrocatalysis, Co_3O_4 could act as an active, stable, and protective base layer, while a NiO coating could be utilized to increase the active surface area.[26,73,81–84]

Successful implementation of hetero-stacks requires a discrete, well-defined interface between the oxide layers. In this work, atomic layer deposition (ALD) is adopted; it can be expected to provide such an interface because it is based on sequential self-limiting surface reactions. This self-limiting nature originates from strong adsorption between the selected precursor and anchoring groups (e.g. hydroxyl) on the underlaying surface. Furthermore, ALD provides an opportunity to work with complex, large surface area substrates that are, for example, required for catalysis. The deposition of NiO using ALD has been successfully demonstrated with various precursors and co-reactants for a range of applications. For example, Koushik et al.[1] deposited NiO using $Ni(^{Me}Cp)_2$ and O_2 plasma for application in solar cells, while Chung et al.[85] adopted $Ni(dmamp)_2$ and H_2O for non-volatile memory devices and Haghverdi Khamene et al.[27] employed $Ni(^tBu\text{-}MeAMD)_2$ and H_2O for NiO serving as an oxygen evolution reaction electrocatalyst. Similarly, Co_3O_4 has been successfully deposited using $CoCp_2$ and O_2 plasma to fabricate anodes for batteries as reported by Donders et al.,[86] while Nandi et al.[87] employed $Co_2(CO)_8$ and O_3 to synthesize Co_3O_4 as a catalyst in $NaBH_4$ hydrolysis.

For templating purposes, a textured film is desired. Donders et al.[88] have demonstrated a preferential (111) orientation for Co_3O_4 films based on $CoCp_2$ and O_2 plasma, whilst the combination of $Ni(^{Me}Cp)_2$ and O_2 plasma has been shown[1,27] to yield a preferential (200) orientation. These processes will therefore be employed to investigate whether the texture of Co_3O_4 and NiO can be tuned by synthesizing thin-film stacks. However, the crystallinity of ALD films and the texture, i.e., the preferred crystallographic growth direction, are influenced by several factors, including the choice of reactant/co-reactant, deposition temperature, impurity level in the film, film thickness, and the choice of substrate.[89] Following the demonstration of the hetero-epitaxial relationship between NiO and Co_3O_4, we will investigate the influence of key process parameters – including the temperature, reactant, and co-reactant – on the growth of NiO on Co_3O_4. This will help identify the optimal ALD process conditions required for achieving hetero-epitaxial growth.

Results and discussion

As an initial step, thin films of the individual oxides on c-Si have been characterised. These films were deposited on c-Si (100) with 2.5 nm native oxide at a substrate table temperature

of 300 °C using previously developed plasma-enhanced ALD processes based on $Ni(^{Me}Cp)_2$ as a precursor for NiO and $CoCp_2$ as a precursor for Co_3O_4 and an O_2 plasma co-reactant for both processes.[1,88,90]

The crystal structures of the films were investigated using X-ray diffraction (XRD) (Fig. 1). Note that the ALD films are typically of polycrystalline nature. The 23 nm NiO film shows a prominent feature at 43.24 ± 0.04°, which is identified as the (200) reflection of the cubic $Fm3m$ (225) rock-salt structure.[71] No other diffraction peaks are observed, implying a strong ⟨100⟩ texture. The derived lattice constant of 4.18 ± 0.01 Å is in close agreement with the theoretical value for NiO of 4.17 Å (ICSD 9866). The XRD pattern of the 51 nm Co_3O_4 film displays two distinct features at 38.52 ± 0.04° and 59.36 ± 0.04°, which are identified as the (222) and (333) peaks of the cubic $Fd3m$ (227) spinel structure.[72] No other peaks are present, indicating a strong ⟨111⟩ texture for spinel Co_3O_4. It is important to note that this texture led to the assignment of the (333) reflection instead of the (115) reflection for the 59° feature. The extracted lattice constant for Co_3O_4, 8.09 ± 0.01 Å, again closely matches the literature value of 8.07 Å (ICSD 36256). Therefore, it can be concluded that both ALD films are polycrystalline under the investigated growth conditions, and have a strong texture.
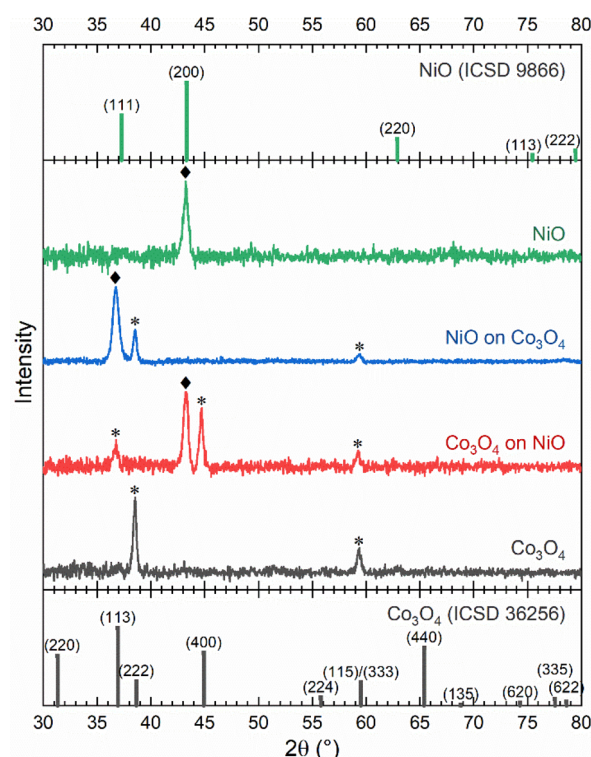

Fig. 1 Goniometric X-ray diffractograms of the c-Si/NiO, c-Si/Co_3O_4, c-Si/NiO/Co_3O_4 and c-Si/Co_3O_4/NiO stacks. Peaks associated with the NiO rock-salt structure are indicated by ◆ and peaks associated with the spinel phase of Co_3O_4 are indicated by *. ICSD reference measurements of both NiO and Co_3O_4 are provided.

Next, hetero-stacks of the oxides were deposited. The c-Si/53 nm Co_3O_4/27 nm NiO stack displays three distinct features in the diffractogram. The peaks at $38.54 \pm 0.04°$ and $59.36 \pm 0.04°$ correspond to those identified in the $\langle 111 \rangle$-textured Co_3O_4 template. The third peak at $36.74 \pm 0.04°$ is attributed to the (111) peak of the NiO rock-salt structure. The sole presence of the NiO (111) peak indicates that the NiO layer adapts its preferred growth direction to follow the $\langle 111 \rangle$ texture of the underlying Co_3O_4 template. Rocking curve XRD analysis of the angular distribution of the Co_3O_4 (111) reflection yields an FWHM of the texture orientation of ~6°. The texture of the NiO overlayer closely matches the distribution of the underlying Co_3O_4 (see the ESI†). The NiO (111) peak position corresponds to a lattice constant of 4.23 ± 0.01 Å, which is significantly larger than the lattice constant observed for NiO directly deposited on c-Si. This out-of-plane elongation of the unit cell is suggested as being attributable to compensation for the compressive strain within the horizontal plane, which facilitates lattice matching between the NiO and Co_3O_4 layers, as the lattice parameter of Co_3O_4 is 1.94 times larger than that of NiO, and equivalent interatomic distances of Co_3O_4 are 0.97 times those of NiO (Table S1†).

Conversely, four features are observed in the diffractogram of the c-Si/29 nm NiO/42 nm Co_3O_4 stack. The feature at $43.28 \pm 0.04°$ is attributed to the (200) reflection of the NiO template. The dominant Co_3O_4 feature at $44.72 \pm 0.04°$ corresponds to the (400) peak of the spinel phase, indicating that Co_3O_4 adjusts its preferred growth direction to align with the underlying $\langle 100 \rangle$-textured NiO template. However, additional features at $36.76 \pm 0.04°$ and $59.28 \pm 0.04°$, attributed to the (113) and (115) reflections of the spinel structure, show the presence of secondary texture components. Furthermore, the lattice constant of 8.10 ± 0.01 Å, associated with the Co_3O_4 features, shows that the Co_3O_4 unit cell is not strained to match with that of NiO.

The crystal growth of the films was further investigated using cross-sectional scanning transmission electron microscopy (STEM) (Fig. 2). The STEM images have been acquired from selected grains that could be imaged along the $\langle 110 \rangle$ zone axis. These images are assumed representative of the whole film. Cross-sectional energy-dispersive X-ray spectroscopy (EDX) elemental mappings of both stacks confirm the deposition of well-defined, compositionally separated homogeneous films. Bright-field STEM images reveal that both Co_3O_4 and NiO grow in a columnar morphology, confirming the polycrystalline nature of the films. Co_3O_4 furthermore displays a larger lateral larger grain size compared to NiO. Based on the bright-field TEM contrast, a larger disorder is observed in the NiO crystals as compared to Co_3O_4 (see also Fig. S1 and S2†).

In both stacks, crystals are observed to continue their growth across the interface. The hetero-epitaxial relationship between the Co_3O_4 template and the NiO film is demonstrated in Fig. 2c and the corresponding fast Fourier transforms (FFT) from selected areas are shown in Fig. 2d and h. Both the FFT patterns are characteristic of $\langle 011 \rangle$ zone-axis patterns. Their identical orientation proves the identical crystallographic orientation of the domains at both sides of the interface. The denser pattern in Fig. 2h reflects the doubled unit cell dimensions of Co_3O_4 compared to NiO. In the atomic resolution image of Fig. 2c, the hetero-epitaxy relationship can also be recognized; horizontal {111} planes of both crystal structures are aligned parallel to the interface, while an additional set of {111} planes at an inclination of 71° continue across the inter-

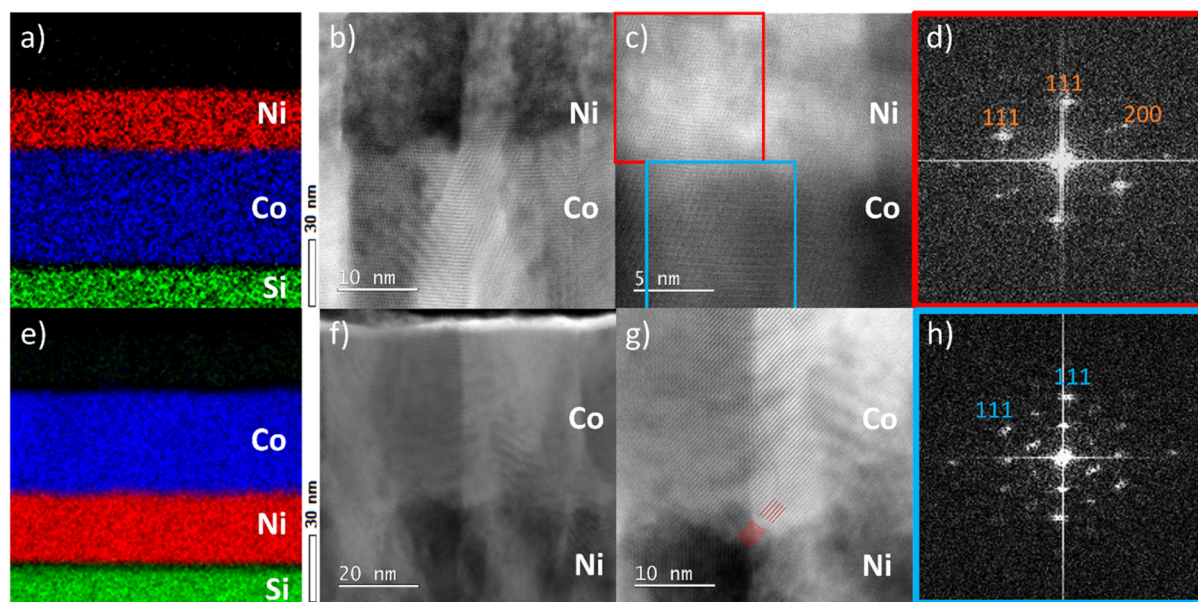**Fig. 2** (a and e) EDX elemental mappings of the stacks. Complementary cross-sectional BF-STEM images of the (b and c) c-Si/Co_3O_4/NiO stack and the (f and g) c-Si/NiO/Co_3O_4 stack. (d and h) The corresponding $\langle 011 \rangle$ zone-axis patterns of (c). The {111} planes of both oxides are indicated in (g).

face. Similarly, detailed images of the c-Si/NiO/Co$_3$O$_4$ stack also reveal the hetero-epitaxial relationship between NiO and Co$_3$O$_4$ grains. This is highlighted in Fig. 2g, where the diagonally oriented {111} planes of NiO and Co$_3$O$_4$ run parallel. Based on the combined XRD and TEM results, we conclude that NiO grows epitaxially on Co$_3$O$_4$ likely in a compressively strained fashion to accommodate lattice mismatch between both layers. Similarly, Co$_3$O$_4$ predominantly grows epitaxially on NiO. However, no strain is observed in the XRD pattern, suggesting that, in this case, the epitaxial relationship is likely facilitated by misfit dislocations at the interface rather than by lattice strain.

As is evident from the TEM results, rock-salt NiO grows on spinel Co$_3$O$_4$ and *vice versa*. From the STEM images, it cannot be concluded whether this phase transition occurs exactly at the interface between the two layers, as the interface between NiO and Co$_3$O$_4$ is not atomically flat in both stacks. Therefore, X-ray photoelectron spectroscopy (XPS) was employed to further investigate the NiO–Co$_3$O$_4$ interface (Fig. 3). Initial measurements of the single oxides on c-Si were performed for reference. NiO exhibits the characteristic 854 eV feature with a shoulder at 856 eV in the Ni 2p spectrum, indicative of the octahedrally coordinated Ni^{2+} states expected for its rock-salt structure.[26,90–94] Co$_3$O$_4$ shows both the Co 2p$_{3/2}$ feature at 779.7 eV and the characteristic spin–orbit splitting of 15.0 eV, which represents the mixed tetrahedral Co^{2+} and octahedral Co^{3+} states characteristic of the spinel structure.[26,90,93–96]

The interface between NiO and Co$_3$O$_4$ has been investigated by depositing layers of NiO from 5, 10, 20, and 40 ALD cycles on a Co$_3$O$_4$ film and *vice versa*. The thickness of the film layers deposited on the template increases with the number of ALD cycles and was calculated using the Thickogram model (see the ESI†). All Ni 2p spectra were corrected for the cobalt oxide Auger features, and all Co 2p spectra were corrected for the nickel oxide Auger features (see the ESI†). NiO growth on Co$_3$O$_4$ was monitored using the Ni 2p spectrum (Fig. 3a). Initially, the 856 eV shoulder is the dominant feature, which is indicative of the presence of Ni^{3+}.[26,90–94] The presence of Ni^{3+} is attributed to the NiO adapting to the underlying Co$_3$O$_4$, which also contains Co^{3+}. This observation aligns well with previous work, where we showed that a supercycle ALD process of NiO and Co$_3$O$_4$ can form both NiCoO$_2$ (rock-salt) and NiCo$_2$O$_4$ (spinel) films depending on the cycle ratio.[90] However, after 20 ALD cycles (~1.0 nm), the 854 eV shoulder becomes dominant again, and after 40 ALD cycles (~2.2 nm), only a small increase in the 856 eV shoulder is observed compared to NiO on c-Si. It can therefore be concluded that the NiO film is affected by the underlying spinel only for the first few ALD cycles (~0.5 nm) and returns to its thermodynamically stable valence state of +2 within the first nanometres of deposition.

Similarly, an increased loss feature is observed between 785 and 790 eV in the Co 2p spectrum at 5 and 10 ALD cycles of Co$_3$O$_4$ on NiO (0.2 and 0.4 nm, respectively). This increase in the loss feature is accompanied by an increased spin–orbit splitting of 15.9 and 15.7 eV, respectively, indicating the presence of octahedrally coordinated Co^{2+} states. However, after 20 ALD cycles (~0.8 nm), the energy split is reduced to 15.2 eV and the loss feature has decreased in intensity, indicating rapid relaxation of Co$_3$O$_4$ in its spinel structure consisting of Co^{2+} and Co^{3+}.[26,90,93–96]

Based on these observations, we can conclude that the crystallographic orientation of NiO can be tuned using a Co$_3$O$_4$ template, and *vice versa*, due to a hetero-epitaxial growth relationship between both materials. The two materials adopt the crystal orientation of the template material but crystallize (almost) directly in their own stable crystal structure, with the corresponding metal atom coordination.

As mentioned in the introduction, an ALD process is characterized by a range of parameters that can be tuned to
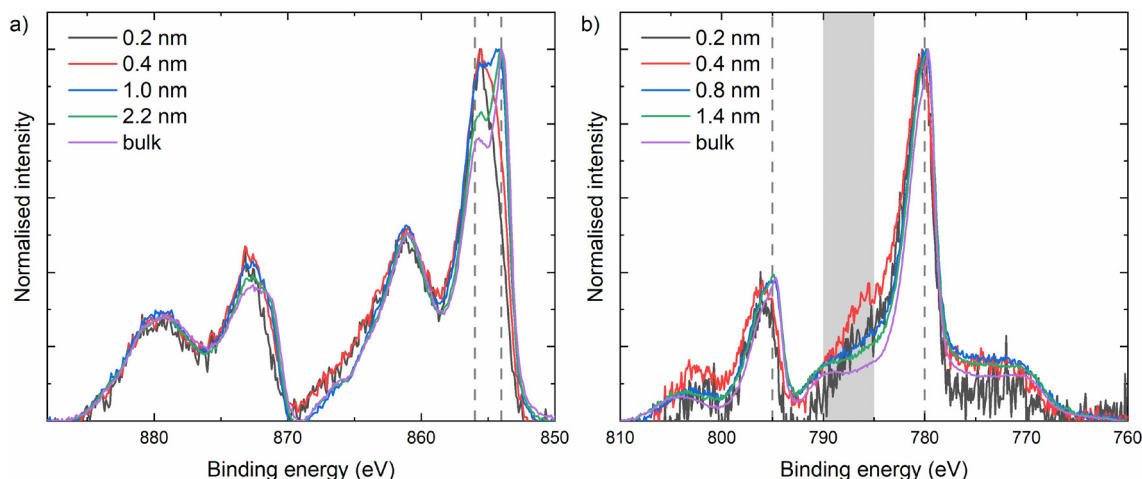

Fig. 3 XPS measurements of films following 5, 10, 20 and 40 ALD cycles of (a) nickel oxide on c-Si/Co$_3$O$_4$ traced using the Ni 2p spectrum and (b) cobalt oxide deposited on c-Si/NiO traced using the Co 2p spectrum. The features at 854 eV and 856 eV are indicated in the Ni 2p spectrum. In the Co 2p spectrum, the 785–790 eV region is highlighted, whilst the dashed lines indicate the 15 eV spin–orbit split.

influence the growth behaviour of the oxides. The most common process parameters, *i.e.*, choice of precursor, co-reactant, and temperature, were varied in this study to evaluate their impact on the epitaxial growth of NiO on Co_3O_4. The influence of ALD parameters on NiO deposited on *c*-Si/native oxide was investigated initially (Fig. 4a and S7†). First, the substrate table temperature was decreased from 300 °C to 150 °C. This caused a slight shift in the (200) XRD peak to lower 2θ, such that the lattice constant slightly increased to 4.20 ± 0.01 Å, suggesting the presence of strain. Next, the precursor was changed to Ni(^{t}Bu-MeAMD)$_2$, while maintaining the 150 °C substrate table temperature. No significant differences were observed between both precursors, as the film also grew in the ⟨100⟩ orientation. The strain observed in both films might be attributed to various factors such as differences in stoichiometry, thermal expansion coefficients, and texture-dependent minimization.[97] At higher substrate temperatures, the strain might be reduced by higher surface mobilities of the adatoms during growth.[89] Finally, the O_2 plasma was replaced with H_2O as a co-reactant in the Ni(^{t}Bu-MeAMD)$_2$-based process at a substrate table temperature of 150 °C. This shifted the texture of the film to ⟨111⟩ with a lattice parameter of 4.21 ± 0.01 Å. It is speculated that the change in the preferred growth direction originates from the presence of hydroxyl groups that stabilize the (111) surface.[98] This is consistent with XPS measurements of the O 1s spectrum (Fig. S8†), which show an increase in the hydroxide shoulder only for the H_2O-based process.

A comparison between the above-mentioned results and those related to NiO deposited on Co_3O_4 (Fig. 4b and S9†) reveals that the tunability of the NiO texture is influenced by the ALD parameters. At a lower deposition temperature (Ni(^{Me}Cp)$_2$ precursor, 150 °C), both the (111) and (200) peaks are observed, indicating an incomplete epitaxial relationship, although the (111) peak remains dominant. Lattice parameters of 4.21 ± 0.01 Å and 4.20 ± 0.01 Å are deduced from the (111) and (200) peaks, respectively, suggesting that the film remains strained, albeit to a lesser extent than that at 300 °C. Similarly, for the plasma-enhanced ALD process based on Ni(^{t}Bu-MeAMD)$_2$, both peaks are present, but the (200) peak is more dominant as compared to that of the Ni(^{Me}Cp)$_2$ film. Interestingly, a distinct difference in the lattice parameters is observed, with 4.23 ± 0.01 Å for the (111) reflection and 4.20 ± 0.01 Å for the (200) reflection. Here, it is important to note that in the goniometric XRD measurements, horizontal lattice planes are probed and the (111) peak originates from a different subset of crystals in the film than the (200) peak. This suggests that the ⟨111⟩-oriented grains grow epitaxially on the Co_3O_4 grains in a strained manner to compensate for the difference in lattice parameters between both structures, while the ⟨200⟩-oriented grains grow independently of the substrate. Additional measurements of a thinner NiO film reveal that the (200) peak is initially not observed (Fig. S10†). It is therefore hypothesized that the epitaxial relationship exists in the initial phase of growth, but the ALD process does not supply enough energy to fully retain the strained epitaxial layer, causing the ⟨100⟩-oriented growth preferred on *c*-Si to develop also in thicker NiO layers.

The NiO film based on Ni(^{t}Bu-MeAMD)$_2$ and H_2O remains fully (111) oriented. However, a shift to higher 2θ is observed compared to the epitaxial (111) orientations of the plasma-based processes. The lattice parameter of 4.19 ± 0.01 Å shows reduced strain compared to deposition on *c*-Si, suggesting that there is no hetero-epitaxial relationship with the underlying Co_3O_4 template. Additional cross-sectional TEM measurements (Fig. S11†) confirm that NiO grains do not evolve as continuation of the Co_3O_4 grains and no epitaxial relationship exists at the interface. This might be related to the absence of the energetic ions generated by the plasma, which potentially stimulate ALD surface reactions. The increased reactivity pro-
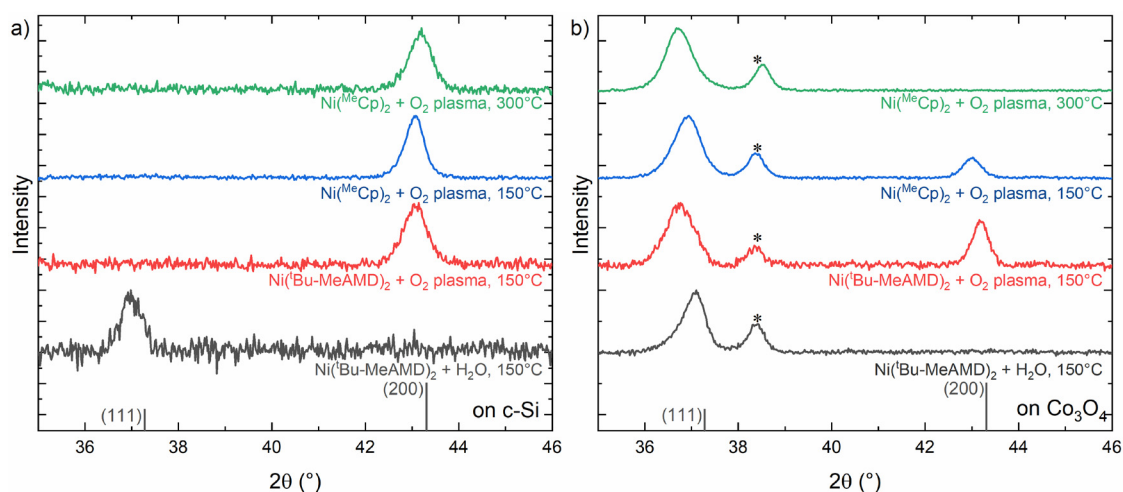

Fig. 4 Goniometric X-ray diffraction patterns of NiO deposited using several ALD processes on (a) *c*-Si and (b) *c*-Si/Co_3O_4. The Co_3O_4 (111) peak is indicated by * and the ICSD database reference of NiO is provided (ICSD 9866).

vided by plasma species reduces the thermal energy required at the substrate to drive ALD surface chemistries and epitaxy.[99,100]
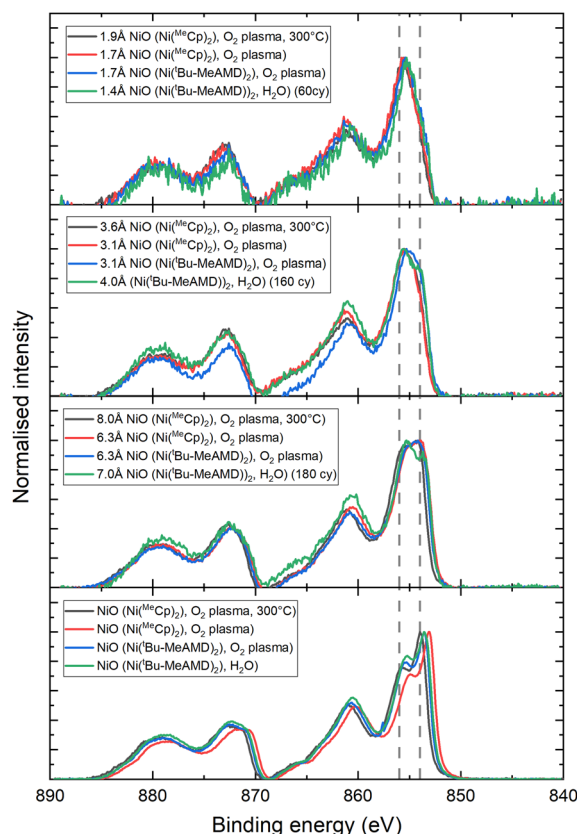

Fig. 5 XPS spectra of various thicknesses of ALD NiO films on *c*-Si/ Co$_3$O$_4$. The features at 854 eV and 856 eV are indicated as a guide to the eye.

Additional XPS studies on the Co$_3$O$_4$–NiO interface were conducted for the several ALD NiO processes to investigate whether differences in epitaxial growth are related to the chemical environment. A comparison of the Ni 2p spectra of the NiO films (on *c*-Si) shows that all films exhibit the expected Ni^{2+} oxidation state. However, both films deposited using the Ni(^{t}Bu-MeAMD)$_2$ precursor show small amounts of nitrogen ($\sim$1.5 at% N/(N + O + Ni)), irrespective of the co-reactant (Fig. S12†). This nitrogen in the H$_2$O process is assigned to the nickel-bonded N in the surface amidinate moiety in line with the study of Zhao *et al.*,[101] whilst the O$_2$ plasma results in nitrate-like bonds.[101,102] The presence of impurities is a known factor preventing crystallization and could therefore partially explain why less epitaxial growth is observed for the plasma process with Ni(^{t}Bu-MeAMD)$_2$ as compared to Ni(^{Me}Cp)$_2$, which has negligible impurity levels.[89,90,103]

Investigation of the nucleation of the NiO layers on Co$_3$O$_4$ reveals that all plasma-based processes show similar growth behaviour (Fig. 5). Initially, NiO nucleates with Ni^{3+} oxidation states, but transitions to the expected Ni^{2+}-based film in the early stage of growth within the first 20 cycles. The H$_2$O process, on the other hand, displays a different nucleation behaviour. Although the sub-monolayer growth is similar, a more defined peak splitting is observed between the main peak and shoulder for thicker films. This could indicate the formation of separate phases, possibly a nickel hydroxide phase, and therefore a more defective growth. Besides the different chemical environments, a major nucleation delay is observed for H$_2$O-based NiO on Co$_3$O$_4$. While a nucleation delay of $\sim$40 cycles is common on *c*-Si, a delay of $\sim$160 cycles is observed on Co$_3$O$_4$ (Fig. S13†). This nucleation delay suggests a defect-driven initial growth as opposed to the epitaxial growth for all other NiO processes.

Conclusions

In this study, we have combined NiO and Co$_3$O$_4$ in heterostructures using ALD to control their crystallographic texture. ALD films based on cyclopentadienyl precursors and an oxygen plasma exhibit strongly textured ⟨100⟩ rock-salt NiO and ⟨111⟩ spinel Co$_3$O$_4$ in a columnar morphology. In the heterostructure, Co$_3$O$_4$ adapts its growth direction to follow the ⟨100⟩ texture of NiO films. Similarly, NiO adapts its crystal orientation to mimic the ⟨111⟩-textured Co$_3$O$_4$. While Co$_3$O$_4$ retains its lattice constant of 8.10 Å when templated on NiO, NiO adapts its out-of-plane lattice constant from 4.18 Å to

Table 1 Thicknesses of the NiO films as presented in Fig. 4, S4, S6 and S7† as determined by spectroscopic ellipsometry

	On Co$_3$O$_4$	On *c*-Si
Ni(^{Me}Cp)$_2$ + O$_2$ plasma, 300 °C	27 nm	23 nm
Ni(^{Me}Cp)$_2$ + O$_2$ plasma, 150 °C	30 nm	40 nm
Ni(^{t}Bu-MeAMD)$_2$ + O$_2$ plasma, 150 °C	31 nm	18 nm
Ni(^{t}Bu-MeAMD)$_2$ + H$_2$O, 150 °C	19 nm	18 nm
Ni(^{t}Bu-MeAMD)$_2$ + O$_2$ plasma, 150 °C (thin, see the ESI†)	11 nm	

Table 2 Elemental concentrations of the films deposited on NiO and Co$_3$O$_4$ films after 40 ALD cycles as determined by RBS

Template	Template thickness (SE) (nm)	40-cycle film	Film thickness (XPS) (nm)	O (TFU)	Co (TFU)	Ni (TFU)	Density of the template (g cm^{-3})
Co$_3$O$_4$	35	NiO	1.4	182 ± 10	129 ± 3	8.0 ± 0.3	5.0 ± 0.3
NiO	21	Co$_3$O$_4$	2.2	128 ± 10	8.0 ± 0.3	106 ± 2.4	6.5 ± 0.6

1 TFU = 10^{15} atoms per cm^2.

4.23 Å to facilitate compressively strained epitaxy with the Co_3O_4 template. XPS reveals that both materials crystallize in their own stable crystal structure with corresponding metal atom coordination within the first 20 ALD cycles.

Variations in the ALD process parameters of NiO growth reveal that the NiO crystal orientation on c-Si is independent of the precursor or temperature but depends on the co-reactant. Switching from O_2 plasma as co-reactant to H_2O shifts the texture to ⟨111⟩. The epitaxial relationship in the stack, however, is more sensitive to ALD parameters. Lowering the substrate table temperatures from 300 °C to 150 °C leads to a partial loss of the ⟨111⟩ texture, such that ⟨100⟩-oriented grains develop when the film is thick enough. This effect is more pronounced for the $Ni(^tBu\text{-}MeAMD)_2$-based films as compared to the $Ni(^{Me}Cp)_2$-based films, possibly due to nitrogen impurities in the film. No epitaxial growth is observed for the H_2O-based process.

In conclusion, we have demonstrated that ALD hetero-stacks offer an effective approach for controlling crystalline texture. Placing our results in perspective, we infer that this method shows strong potential for achieving crystallographic control of thin films on templates relevant for practical applications. This work therefore reveals an additional merit of ALD beyond established benefits such as thickness control, precise composition tuning, and excellent uniformity and conformality. It expands the ALD toolbox to include crystallographic control, opening new opportunities for the design and engineering of thin films.

Experimental methods

All NiO and Co_3O_4 films were deposited using a home-built plasma-enhanced ALD reactor described elsewhere.[104] The system features an inductively coupled plasma source powered at 13.56 MHz. The pumping system consists of a turbomolecular pump paired with a rotary vane pump, capable of reaching a base pressure below 1×10^{-6} mbar. The reactors walls were heated to 100 °C, whilst the 4-inch wafer-based substrate holder temperature was varied between 300 °C and 150 °C, as indicated in the manuscript. Cobaltocene ($CoCp_2$, 98% purity, ACROS Organics) was placed in a stainless steel cylindrical bubbler and heated to 80 °C and introduced into the chamber using an argon carrier gas through a line at 100 °C. Similarly, 1,1′-dimethylnickelocene ($Ni(^{Me}Cp)_2$, 97% purity, Sigma-Aldrich) was heated to 55 °C and delivered to the chamber using argon gas through a line at 75 °C. Both precursors reacted with a 100 W O_2 plasma co-reactant. Both precursors were introduced using a 4 s/4 s/5 s precursor dosing/Ar purge/pump sequence with x s/1 s/3 s O_2 plasma exposure/O_2 purge/pump sequence, where $x = 3$ s for NiO deposition and $x = 5$ s for Co_3O_4 deposition.[1,26,88,90] All films were deposited on c-Si (100) with 15 minutes of O_2 plasma treatment before deposition. Hetero-stacks were deposited without breaking the vacuum to ensure a clean interface.

Additional NiO deposition processes were based on the bis (N,N′-di-t-butylacetamidinato)nickel precursor ($Ni(^tBu\text{-}MeAMD)_2$, 99.999% purity, STREM) contained in a stainless steel cylindrical container heated to 90 °C and delivered using Ar through a line heated to 120 °C. In both processes, the precursor is delivered by 2× (3 s precursor dose + 2 s Ar line purge) followed by a 20 s pump. Afterwards, either an O_2 plasma/O_2 purge/purge of 5 s/1 s/10 s or a H_2O/pump of 1 s/60 s was used. The thicknesses of the various NiO films are presented in Table 1.

The crystallography of the films was investigated using a Bruker Discover D8 (Cu K_α radiation, $\lambda = 1.54060$ Å) in goniometric XRD mode at an axis offset of 3° to remove c-Si substrate peaks (Fig. S14†). Measurements in the 2θ range from 30.00–80.00° were performed with a step size of 0.04° at an integration time of 1 s, whilst measurements in the 2θ range from 34.00–46.00° were performed with a step size of 0.02° at an integration time of 4 s.

X-ray photoelectron spectroscopy measurements were performed using a Thermo Scientific KA 1066 spectrometer with monochromatic Al K_α X-rays. The binding axis was calibrated by the 248.8 eV adventitious C 1s peak. Thickness values were determined from the XPS data using a Thickogram model based on the Ni 3p (66.6 eV) and Co 3p (59.1 eV) features. The attenuation length was determined using the Tanuma–Powell–Penn-2M method, with a bandgap of 2 eV[105] and a density of 5.0 g cm^{-3} for Co_3O_4. For NiO, a bandgap of 3.8 eV[1] was used in combination with a density of 6.5 g cm^{-3} for plasma NiO and a density of 5.1 g cm^{-3} for thermal NiO[2]. Densities of NiO (plasma, $Ni(^{Me}Cp)_2$, 300 °C) and Co_3O_4 were determined by Rutherford backscattering spectrometry (RBS) (Table 2). RBS was carried out by Detect99 using a 200 keV He$^+$ beam at perpendicular incidence and two detectors at scattering angles of 170° and 107°. Channel mode was used to reduce the background under the oxygen peaks. PIXE was used to distinguish Co from Ni. For PIXE, a 2.7 MeV H$^+$ beam was applied at perpendicular incidence. The X-ray detector was positioned at an angle of 45° between the beam and the specimen normal, and 30 μm Kapton was used as an absorber. The PIXE spectra were analysed with the Gupix[106] PIXE simulation package, and the resulting Co/Ni ratio was entered as a Co_xNi_y "molecule" in the WiNDF[107] RBS simulation package to determine the absolute amounts. Electron microscopy images were acquired using a probe-corrected JEOL ARM 200F transmission electron microscope operated at 200 kV equipped with a 100 mm^2 Centurio SDD EDX detector. Cross-sectional TEM samples were made using a focused ion beam (FIB) following a standard lift-out sample preparation protocol.

Data availability

The data that support the findings of this study are openly available in Zenodo at **https://doi.org/10.5281/zenodo.14160831**.

Conflicts of interest

There are no conflicts to declare.

Acknowledgements

References

1 D. Koushik, M. Jošt, A. Dučinskas, C. Burgess, V. Zardetto, C. Weijtens, M. A. Verheijen, W. M. M. Kessels, S. Albrecht and M. Creatore, Plasma-Assisted Atomic Layer Deposition of Nickel Oxide as Hole Transport Layer for Hybrid Perovskite Solar Cells, *J. Mater. Chem. C*, 2019, **7**(40), 12532–12543, DOI: **10.1039/C9TC04282B**.

2 N. Phung, D. Zhang, C. van Helvoirt, M. Verhage, M. Verheijen, V. Zardetto, F. Bens, C. H. L. Weijtens, L. J. Geerligs, W. M. M. Kessels, B. Macco and M. Creatore, Atomic Layer Deposition of NiO Applied in a Monolithic Perovskite/PERC Tandem Cell, *Sol. Energy Mater. Sol. Cells*, 2023, **261**, 112498, DOI: **10.1016/j.solmat.2023.112498**.

3 E. A. Gibson, A. L. Smeigh, L. Le Pleux, J. Fortage, G. Boschloo, E. Blart, Y. Pellegrin, F. Odobel, A. Hagfeldt and L. Hammarström, A P–Type NiO–Based Dye–Sensitized Solar Cell with an Open–Circuit Voltage of 0.35 V, *Angew. Chem.*, 2009, **121**(24), 4466–4469, DOI: **10.1002/ange.200900423**.

4 X. Xia, J. Tu, Y. Zhang, X. Wang, C. Gu, X. B. Zhao and H. J. Fan, High-Quality Metal Oxide Core/Shell Nanowire Arrays on Conductive Substrates for Electrochemical Energy Storage, *ACS Nano*, 2012, **6**(6), 5531–5538, DOI: **10.1021/nn301454q**.

5 X. Wang, A. Hu, C. Meng, C. Wu, S. Yang and X. Hong, Recent Advance in Co3O4 and Co3O4-Containing Electrode Materials for High-Performance Supercapacitors, *Molecules*, 2020, **25**(2), 269, DOI: **10.3390/molecules25020269**.

6 F. I. Dar, K. R. Moonoosawmy and M. Es-Souni, Morphology and Property Control of NiO Nanostructures for Supercapacitor Applications, *Nanoscale Res. Lett.*, 2013, **8**(1), 363, DOI: **10.1186/1556-276X-8-363**.

7 J. Xu, L. Gao, J. Cao, W. Wang and Z. Chen, Preparation and Electrochemical Capacitance of Cobalt Oxide (Co3O4) Nanotubes as Supercapacitor Material, *Electrochim. Acta*, 2010, **56**(2), 732–736, DOI: **10.1016/j.electacta.2010.09.092**.

8 Y.-M. Wang, X. Zhang, C.-Y. Guo, Y.-Q. Zhao, C.-L. Xu and H.-L. Li, Controllable Synthesis of 3D NiχCo1−χ Oxides with Different Morphologies for High-Capacity Supercapacitors, *J. Mater. Chem. A*, 2013, **1**(42), 13290, DOI: **10.1039/c3ta12713c**.

9 P. Giannakou, M. G. Masteghin, R. C. T. Slade, S. J. Hinder and M. Shkunov, Energy Storage on Demand: Ultra-High-Rate and High-Energy-Density Inkjet-Printed NiO Micro-Supercapacitors, *J. Mater. Chem. A*, 2019, **7**(37), 21496–21506, DOI: **10.1039/C9TA07878A**.

10 H. Zhang, Y. Chen, W. Wang, G. Zhang, M. Zhuo, H. Zhang, T. Yang, Q. Li and T. Wang, Hierarchical Mo-Decorated Co3O4 Nanowire Arrays on Ni Foam Substrates for Advanced Electrochemical Capacitors, *J. Mater. Chem. A*, 2013, **1**(30), 8593, DOI: **10.1039/c3ta11152k**.

11 H. Steinebach, S. Kannan, L. Rieth and F. Solzbacher, H2 Gas Sensor Performance of NiO at High Temperatures in Gas Mixtures, *Sens. Actuators, B*, 2010, **151**(1), 162–168, DOI: **10.1016/j.snb.2010.09.027**.

12 I. Hotovy, V. Rehacek, P. Siciliano, S. Capone and L. Spiess, Sensing Characteristics of NiO Thin Films as NO2 Gas Sensor, *Thin Solid Films*, 2002, **418**(1), 9–15, DOI: **10.1016/S0040-6090(02)00579-5**.

13 J. M. Xu and J. P. Cheng, The Advances of Co 3 O 4 as Gas Sensing Materials: A Review, *J. Alloys Compd.*, 2016, **686**, 753–768, DOI: **10.1016/j.jallcom.2016.06.086**.

14 A. Shanmugasundaram, N. D. Chinh, Y.-J. Jeong, T. F. Hou, D.-S. Kim, D. Kim, Y.-B. Kim and D.-W. Lee, Hierarchical Nanohybrids of B- and N-Codoped Graphene/Mesoporous NiO Nanodisks: An Exciting New Material for Selective Sensing of H 2 S at near Ambient Temperature, *J. Mater. Chem. A*, 2019, **7**(15), 9263–9278, DOI: **10.1039/C9TA00755E**.

15 B. Varghese, M. V. Reddy, Z. Yanwu, C. S. Lit, T. C. Hoong, G. V. Subba Rao, B. V. R. Chowdari, A. T. S. Wee, C. T. Lim and C.-H. Sow, Fabrication of NiO Nanowall Electrodes for High Performance Lithium Ion Battery, *Chem. Mater.*, 2008, **20**(10), 3360–3367, DOI: **10.1021/cm703512k**.

16 Y.-M. Kang, M.-S. Song, J.-H. Kim, H.-S. Kim, M.-S. Park, J.-Y. Lee, H. K. Liu and S. X. Dou, A Study on the Charge–Discharge Mechanism of Co3O4 as an Anode for the Li Ion Secondary Battery, *Electrochim. Acta*, 2005, **50**(18), 3667–3673, DOI: **10.1016/j.electacta.2005.01.012**.

17 S.-L. Chou, J.-Z. Wang, H.-K. Liu and S.-X. Dou, Electrochemical Deposition of Porous Co3O4 Nanostructured Thin Film for Lithium-Ion Battery, *J. Power Sources*, 2008, **182**(1), 359–364, DOI: **10.1016/j.jpowsour.2008.03.083**.

18 A.-U. Rehman, M. Iftikhar, S. Latif, V. Jevtovic, I. M. Ashraf, A. A. El-Zahhar, E. A. Musad Saleh and S. Mustansar Abbas, Current Advances and Prospects in NiO-Based Lithium-Ion Battery Anodes, *Sustainable Energy*

Technol. Assess., 2022, **53**(PA), 102376, DOI: **10.1016/j. seta.2022.102376**.

19 Y. Liu and X. Zhang, Effect of Calcination Temperature on the Morphology and Electrochemical Properties of Co3O4 for Lithium-Ion Battery, *Electrochim. Acta*, 2009, **54**(17), 4180–4185, DOI: **10.1016/j. electacta.2009.02.060**.

20 C.-F. Cheng, Y.-M. Chen, F. Zou, K.-C. Yang, T.-Y. Lin, K. Liu, C.-H. Lai, R.-M. Ho and Y. Zhu, Nanoporous Gyroid Ni/NiO/C Nanocomposites from Block Copolymer Templates with High Capacity and Stability for Lithium Storage, *J. Mater. Chem. A*, 2018, **6**(28), 13676–13684, DOI: **10.1039/C8TA04077J**.

21 Y. Zhu, H. Guo, Y. Wu, C. Cao, S. Tao and Z. Wu, Surface-Enabled Superior Lithium Storage of High-Quality Ultrathin NiO Nanosheets, *J. Mater. Chem. A*, 2014, **2**(21), 7904, DOI: **10.1039/c4ta00257a**.

22 W. Hao, S. Chen, Y. Cai, L. Zhang, Z. Li and S. Zhang, Three-Dimensional Hierarchical Pompon-like Co3O4 Porous Spheres for High-Performance Lithium-Ion Batteries, *J. Mater. Chem. A*, 2014, **2**(34), 13801–13804, DOI: **10.1039/c4ta02012j**.

23 X. Xu, X. Hou, P. Du, C. Zhang, S. Zhang, H. Wang, A. Toghan and M. Huang, Controllable Ni/NiO Interface Engineering on N-Doped Carbon Spheres for Boosted Alkaline Water-to-Hydrogen Conversion by Urea Electrolysis, *Nano Res.*, 2022, **15**(8), 7124–7133, DOI: **10.1007/s12274-022-4505-1**.

24 J. Xiao, X. Zhang, T. Gao, C. Zhou and D. Xiao, Electrochemical Formation of Multilayered NiO Film/Ni Foam as a High-Efficient Anode for Methanol Electrolysis, *J. Solid State Electrochem.*, 2017, **21**(8), 2301–2311, DOI: **10.1007/s10008-017-3570-y**.

25 G. Ma, X. Zhang, G. Zhou and X. Wang, Hydrogen Production from Methanol Reforming Electrolysis at NiO Nanosheets Supported Pt Nanoparticles, *Chem. Eng. J.*, 2021, **411**, DOI: **10.1016/j.cej.2020.128292**.

26 R. T. M. van Limpt, M. Lao, M. N. Tsampas and M. Creatore, Unraveling the Role of the Stoichiometry of Atomic Layer Deposited Nickel Cobalt Oxides on the Oxygen Evolution Reaction, *Adv. Sci.*, 2024, **11**(32), 1–11, DOI: **10.1002/advs.202405188**.

27 S. Haghverdi Khamene, C. van Helvoirt, M. N. Tsampas and M. Creatore, Electrochemical Activation of Atomic-Layer-Deposited Nickel Oxide for Water Oxidation, *J. Phys. Chem. C*, 2023, **127**(46), 22570–22582, DOI: **10.1021/acs. jpcc.3c05002**.

28 R. Dutta, A. Maity, A. Marsicano, M. Ceretti, D. Chernyshov, A. Bosak, A. Villesuzanne, G. Roth, G. Perversi and W. Paulus, Long-Range Oxygen Ordering Linked to Topotactic Oxygen Release in Pr 2 NiO 4+δ Fuel Cell Cathode Material, *J. Mater. Chem. A*, 2020, **8**(28), 13987–13995, DOI: **10.1039/D0TA04652C**.

29 W. Dai, X. Bai, Y. A. Zhu, Y. Zhang, T. Lu, Y. Pan and J. Wang, Surface Reconstruction Inducedin Situphosphorus Doping in Nickel Oxides for an Enhanced Oxygen Evolution Reaction, *J. Mater. Chem. A*, 2021, **9**(10), 6432–6441, DOI: **10.1039/d0ta10925h**.

30 C. Zhang, F. Zheng, Z. Zhang, D. Xiang, C. Cheng, Z. Zhuang, P. Li, X. Li and W. Chen, Fabrication of Hollow Pompon-like Co 3 O 4 Nanostructures with Rich Defects and High-Index Facet Exposure for Enhanced Oxygen Evolution Catalysis, *J. Mater. Chem. A*, 2019, **7**(15), 9059–9067, DOI: **10.1039/C9TA00330D**.

31 H. Sun, H. M. Ang, M. O. Tadé and S. Wang, Co3O4 Nanocrystals with Predominantly Exposed Facets: Synthesis, Environmental and Energy Applications, *J. Mater. Chem. A*, 2013, **1**(46), 14427, DOI: **10.1039/ c3ta12960h**.

32 X. Li, X. Su, Y. Pei, J. Liu, X. Zheng, K. Tang, G. Guan and X. Hao, Generation of Edge Dislocation Defects in Co 3 O 4 Catalysts: An Efficient Tactic to Improve Catalytic Activity for Oxygen Evolution, *J. Mater. Chem. A*, 2019, **7**(17), 10745–10750, DOI: **10.1039/C9TA01697J**.

33 S. Tong, M. Zheng, Y. Lu, Z. Lin, J. Li, X. Zhang, Y. Shi, P. He and H. Zhou, Mesoporous NiO with a Single-Crystalline Structure Utilized as a Noble Metal-Free Catalyst for Non-Aqueous Li-O2 Batteries, *J. Mater. Chem. A*, 2015, **3**(31), 16177–16182, DOI: **10.1039/c5ta03685b**.

34 C. W. Kim, Y. S. Son, A. U. Pawar, M. J. Kang, J. Y. Zheng, V. Sharma, P. Mohanty and Y. S. Kang, Facile Fabrication and Photoelectrochemical Properties of a One Axis-Oriented NiO Thin Film with a (111) Dominant Facet, *J. Mater. Chem. A*, 2014, **2**(46), 19867–19872, DOI: **10.1039/ C4TA03606A**.

35 H. Wu, J. Geng, P. Han, H. Ge, A. M. Alenizi and G. Zheng, Unconventional Mesoporous Single Crystalline NiO by Synergistically Controlled Evaporation and Hydrolysis, *J. Mater. Chem. A*, 2017, **5**(45), 23840–23843, DOI: **10.1039/C7TA08155C**.

36 M. Zheng, H. Dong, Y. Xiao, H. Hu, C. He, Y. Liang, B. Lei, L. Sun and Y. Liu, Hierarchical NiO Mesocrystals with Tuneable High-Energy Facets for Pseudocapacitive Charge Storage, *J. Mater. Chem. A*, 2017, **5**(15), 6921–6927, DOI: **10.1039/C7TA00978J**.

37 W. Bao, R. Wang, B. Li, C. Qian, Z. Zhang, J. Li and F. Liu, Stable Alkali Metal Anodes Enabled by Crystallographic Optimization - a Review, *J. Mater. Chem. A*, 2021, **9**(37), 20957–20984, DOI: **10.1039/d1ta05394a**.

38 A. Hermawan, A. T. Hanindriyo, K. Hongo, R. Maezono and S. Yin, Impact of Surface Faceting on Gas Sensing Selectivity of NiO: Revealing the Adsorption Sites of Organic Vapors on the {111} Facet, *J. Phys. Chem. C*, 2022, **126**(18), 8037–8046, DOI: **10.1021/acs.jpcc.2c00092**.

39 T. Yu, Z. Li, H. Zheng, L. Chen, W. Song, Z. Zhao, J. Li and J. Liu, The Nature of Ni-O Pairs for Ethane Activation on NiO(100) and NiO(110) Surfaces, *Mol. Catal.*, 2019, **474**, 110417, DOI: **10.1016/j.mcat.2019.110417**.

40 R. Gao, J. Zhu, X. Xiao, Z. Hu, J. Liu and X. Liu, Facet-Dependent Electrocatalytic Performance of Co3O4 for Rechargeable Li-O2 Battery, *J. Phys. Chem. C*, 2015, **119**(9), 4516–4523, DOI: **10.1021/jp511363p**.

41 Y. Zeng, T. Li, J. Zhong, H. Mao, M. Fu, D. Ye and Y. Hu, Unraveling the Role of Co3O4 Facet for Photothermal Catalytic Oxidation of Methanol *via* Operando Spectroscopy and Theoretical Investigation, *J. Colloid Interface Sci.*, 2023, **643**, 360–372, DOI: **10.1016/j. jcis.2023.04.046**.

42 Z. Liu, H. M. A. Amin, Y. Peng, M. Corva, R. Pentcheva and K. Tschulik, Facet-Dependent Intrinsic Activity of Single Co3O4 Nanoparticles for Oxygen Evolution Reaction, *Adv. Funct. Mater.*, 2023, **33**(1), 1–8, DOI: **10.1002/adfm.202210945**.

43 E. M. Davis, A. Bergmann, H. Kuhlenbeck and B. Roldan Cuenya, Facet Dependence of the Oxygen Evolution Reaction on Co3O4, CoFe2O4, and Fe3O4 Epitaxial Film Electrocatalysts, *J. Am. Chem. Soc.*, 2024, **146**(20), 13770–13782, DOI: **10.1021/jacs.3c13595**.

44 T. Wiegmann, I. Pacheco, F. Reikowski, J. Stettner, C. Qiu, M. Bouvier, M. Bertram, F. Faisal, O. Brummel, J. Libuda, J. Drnec, P. Allongue, F. Maroun and O. M. Magnussen, Operando Identification of the Reversible Skin Layer on Co 3 O 4 as a Three-Dimensional Reaction Zone for Oxygen Evolution, *ACS Catal.*, 2022, **12**(6), 3256–3268, DOI: **10.1021/acscatal.1c05169**.

45 R. Poulain, A. Klein and J. Proost, Electrocatalytic Properties of (100)-, (110)-, and (111)-Oriented NiO Thin Films toward the Oxygen Evolution Reaction, *J. Phys. Chem. C*, 2018, **122**(39), 22252–22263, DOI: **10.1021/acs. jpcc.8b05790**.

46 M. Burriel, G. Garcia, J. Santiso, A. Abrutis, Z. Saltyte and A. Figueras, Growth Kinetics, Composition, and Morphology of Co3O4 Thin Films Prepared by Pulsed Liquid-Injection MOCVD, *Chem. Vap. Deposition*, 2005, **11**(2), 106–111, DOI: **10.1002/cvde.200406320**.

47 M. Burriel, G. Garcia, J. Santiso, A. N. Hansson, S. Linderoth and A. Figueras, Co3O4 Protective Coatings Prepared by Pulsed Injection Metal Organic Chemical Vapour Deposition, *Thin Solid Films*, 2005, **473**(1), 98–103, DOI: **10.1016/j.tsf.2004.07.081**.

48 F. F. Ferreira, M. H. Tabacniks, M. C. A. Fantini, I. C. Faria and A. Gorenstein, Electrochromic Nickel Oxide Thin Films Deposited under Different Sputtering Conditions, *Solid State Ionics*, 1996, **86–88**(Part 2), 971–976, DOI: **10.1016/0167-2738(96)00236-6**.

49 S.-Y. Han, D.-H. Lee, Y.-J. Chang, S.-O. Ryu, T.-J. Lee and C.-H. Chang, The Growth Mechanism of Nickel Oxide Thin Films by Room-Temperature Chemical Bath Deposition, *J. Electrochem. Soc.*, 2006, **153**(6), C382, DOI: **10.1149/1.2186767**.

50 B. T. Raut, S. G. Pawar, M. A. Chougule, S. Sen and V. B. Patil, New Process for Synthesis of Nickel Oxide Thin Films and Their Characterization, *J. Alloys Compd.*, 2011, **509**(37), 9065–9070, DOI: **10.1016/j.jallcom.2011.06.029**.

51 H. L. Chen, Y. M. Lu and W. S. Hwang, Characterization of Sputtered NiO Thin Films, *Surf. Coatings Technol.*, 2005, **198**(1–3 SPEC. ISS.), 138–142, DOI: **10.1016/j. surfcoat.2004.10.032**.

52 L. Berkat, L. Cattin, A. Reguig, M. Regragui and J. C. Bernède, Comparison of the Physico-Chemical Properties of NiO Thin Films Deposited by Chemical Bath Deposition and by Spray Pyrolysis, *Mater. Chem. Phys.*, 2005, **89**(1), 11–20, DOI: **10.1016/j. matchemphys.2004.07.005**.

53 V. R. Shinde, S. B. Mahadik, T. P. Gujar and C. D. Lokhande, Supercapacitive Cobalt Oxide (Co3O4) Thin Films by Spray Pyrolysis, *Appl. Surf. Sci.*, 2006, **252**(20), 7487–7492, DOI: **10.1016/j.apsusc.2005.09.004**.

54 L. D. Kadam and P. S. Patil, Thickness-Dependent Properties of Sprayed Cobalt Oxide Thin Films, *Mater. Chem. Phys.*, 2001, **68**(1–3), 225–232, DOI: **10.1016/S0254-0584(00)00367-9**.

55 K. Shalini, A. U. Mane, S. A. Shivashankar, M. Rajeswari and S. Choopun, Epitaxial Growth of Co3O4 Films by Low Temperature, Low Pressure Chemical Vapour Deposition, *J. Cryst. Growth*, 2001, **231**(1–2), 242–247, DOI: **10.1016/ S0022-0248(01)01493-2**.

56 L. M. Apátiga and V. M. Castaño, Magnetic Behavior of Cobalt Oxide Films Prepared by Pulsed Liquid Injection Chemical Vapor Deposition from a Metal-Organic Precursor, *Thin Solid Films*, 2006, **496**(2), 576–579, DOI: **10.1016/j.tsf.2005.08.344**.

57 M. Rooth, E. Lindahl and A. Hårsta, Atomic Layer Deposition of Co3O4 Thin Films Using a CoI2/O2 Precursor Combination, *Chem. Vap. Deposition*, 2006, **12**(4), 209–213, DOI: **10.1002/cvde.200506447**.

58 S. R. Nalage, M. A. Chougule, S. Sen, P. B. Joshi and V. B. Patil, Sol-Gel Synthesis of Nickel Oxide Thin Films and Their Characterization, *Thin Solid Films*, 2012, **520**(15), 4835–4840, DOI: **10.1016/j.tsf.2012.02.072**.

59 A. A. Al-Ghamdi, W. E. Mahmoud, S. J. Yaghmour and F. M. Al-Marzouki, Structure and Optical Properties of Nanocrystalline NiO Thin Film Synthesized by Sol-Gel Spin-Coating Method, *J. Alloys Compd.*, 2009, **486**(1–2), 9–13, DOI: **10.1016/j.jallcom.2009.06.139**.

60 J. K. Kang and S. W. Rhee, Chemical Vapor Deposition of Nickel Oxide Films from Ni(C5H5)2/O2, *Thin Solid Films*, 2001, **391**(1), 57–61, DOI: **10.1016/S0040-6090(01) 00962-2**.

61 R. Attri, D. P. Panda, J. Ghatak and C. N. R. Rao, High Crystalline Epitaxial Thin Films of NiO by Plasma-Enhanced ALD and Their Properties, *APL Mater.*, 2023, **11**(9), DOI: **10.1063/5.0157628**.

62 Y. Wang, J. Ghanbaja, P. Boulet, D. Horwat and J. F. Pierson, Growth, Interfacial Microstructure and Optical Properties of NiO Thin Films with Various Types of Texture, *Acta Mater.*, 2019, **164**, 648–653, DOI: **10.1016/ j.actamat.2018.11.018**.

63 E. Lindahl, J. Lu, M. Ottosson and J. O. Carlsson, Epitaxial NiO (100) and NiO (111) Films Grown by Atomic Layer Deposition, *J. Cryst. Growth*, 2009, **311**(16), 4082–4088, DOI: **10.1016/j.crysgro.2009.06.030**.

64 K. B. Klepper, O. Nilsen and H. Fjellvåg, Epitaxial Growth of Cobalt Oxide by Atomic Layer Deposition, *J. Cryst.*

Growth, 2007, **307**(2), 457–465, DOI: **10.1016/j.jcrysgro.2007.06.028**.

65 H. G. Chen, H. S. Wang, S. R. Jian, T. L. Yeh and J. Y. Feng, Epitaxial Growth of Cobalt Oxide Thin Films on Sapphire Substrates Using Atmospheric Pressure Mist Chemical Vapor Deposition, *Coatings*, 2023, **13**(11), DOI: **10.3390/coatings13111878**.

66 C. A. F. Vaz, V. E. Henrich, C. H. Ahn and E. I. Altman, Growth and Characterization of Thin Epitaxial Co3O4 (111) Films, *J. Cryst. Growth*, 2009, **311**(9), 2648–2654, DOI: **10.1016/j.jcrysgro.2009.03.006**.

67 A. U. Mane, K. Shalini, A. Wohlfart, A. Devi and S. A. Shivashankar, Strongly Oriented Thin Films of Co3O4 Deposited on Single-Crystal MgO(100) by Low-Pressure, Low-Temperature MOCVD, *J. Cryst. Growth*, 2002, **240**(1–2), 157–163, DOI: **10.1016/S0022-0248(02)00860-6**.

68 S. Battiato, M. M. Giangregorio, M. R. Catalano, R. Lo Nigro, M. Losurdo and G. Malandrino, Morphology-Controlled Synthesis of NiO Films: The Role of the Precursor and the Effect of the Substrate Nature on the Films' Structural/Optical Properties, *RSC Adv.*, 2016, **6**(37), 30813–30823, DOI: **10.1039/c6ra05510a**.

69 R. Molaei, R. Bayati and J. Narayan, Crystallographic Characteristics and P-Type to n-Type Transition in Epitaxial Nio Thin Film, *Cryst. Growth Des.*, 2013, **13**(12), 5459–5465, DOI: **10.1021/cg401408f**.

70 P. Yang, L. Li, S. Yu, H. Zheng and W. Peng, The Annealing Temperature and Films Thickness Effect on the Surface Morphology, Preferential Orientation and Dielectric Property of NiO Films, *Appl. Surf. Sci.*, 2019, **493**, 396–403, DOI: **10.1016/j.apsusc.2019.06.223**.

71 S. Sasaki, K. Fujino and Y. Takéuchi, X-Ray, Determination of Electron-Density Distributions in Oxides, MgO, MnO, CoO, and NiO, and Atomic Scattering Factors of Their Constituent Atoms, *Proc. Jpn. Acad., Ser. B*, 1979, **55**(2), 43–48, DOI: **10.2183/pjab.55.43**.

72 J. P. Picard, G. Baud, J. P. Besse and R. Chevalier, Croissance Cristalline et Étude Structurale de Co3O4, *J. Less-Common Met.*, 1980, **75**(1), 99–104, DOI: **10.1016/0022-5088(80)90373-2**.

73 J. Zhang, J. Qian, J. Ran, P. Xi, L. Yang and D. Gao, Engineering Lower Coordination Atoms onto NiO/Co3O4 Heterointerfaces for Boosting Oxygen Evolution Reactions, *ACS Catal.*, 2020, **10**(21), 12376–12384, DOI: **10.1021/acscatal.0c03756**.

74 C. Lou, H. Pan, H. Mei, G. Lu, X. Liu and J. Zhang, Low Coordination States in Co3O4/NiOx Heterostructures by Atomic Layer Deposition for Enhanced Gas Detection, *Chem. Eng. J.*, 2022, **448**, 137641, DOI: **10.1016/j.cej.2022.137641**.

75 S. Adhikari, S. Selvaraj, S. H. Ji and D. H. Kim, Encapsulation of Co3O4 Nanocone Arrays *via* Ultrathin NiO for Superior Performance Asymmetric Supercapacitors, *Small*, 2020, **16**(48), 1–13, DOI: **10.1002/smll.202005414**.

76 D. Nam and J. Kim, Development of NiO/Co3O4 Nanohybrids Catalyst with Oxygen Vacancy for Oxygen Evolution Reaction Enhancement in Alkaline Solution, *Int. J. Hydrogen Energy*, 2022, **47**(38), 16900–16907, DOI: **10.1016/j.ijhydene.2022.03.177**.

77 A. Q. Mugheri, A. Tahira, U. Aftab, M. I. Abro, S. R. Chaudhry, L. Amaral and Z. H. Ibupoto, Co3O4/NiO Bifunctional Electrocatalyst for Water Splitting, *Electrochim. Acta*, 2019, **306**, 9–17, DOI: **10.1016/j.electacta.2019.03.092**.

78 Y. Wang, M. Kong, Z. Liu, C. Lin and Y. Zeng, Morella-Rubra-like Metal–Organic-Framework-Derived Multilayered Co3O4/NiO/C Hybrids as High-Performance Anodes for Lithium Storage, *J. Mater. Chem. A*, 2017, **5**(46), 24269–24274, DOI: **10.1039/C7TA08264A**.

79 K. Xu, R. Zou, W. Li, Y. Xue, G. Song, Q. Liu, X. Liu and J. Hu, Self-Assembling Hybrid NiO/Co3O4 Ultrathin and Mesoporous Nanosheets into Flower-like Architectures for Pseudocapacitance, *J. Mater. Chem. A*, 2013, **1**(32), 9107, DOI: **10.1039/c3ta11099k**.

80 X. Yin, C. Zhi, W. Sun, L.-P. Lv and Y. Wang, Multilayer NiO@Co3O4@graphene Quantum Dots Hollow Spheres for High-Performance Lithium-Ion Batteries and Supercapacitors, *J. Mater. Chem. A*, 2019, **7**(13), 7800–7814, DOI: **10.1039/C8TA11982A**.

81 M. B. Stevens, L. J. Enman, E. H. Korkus, J. Zaffran, C. D. M. Trang, J. Asbury, M. G. Kast, M. C. Toroker and S. W. Boettcher, Ternary Ni-Co-Fe Oxyhydroxide Oxygen Evolution Catalysts: Intrinsic Activity Trends, Electrical Conductivity, and Electronic Band Structure, *Nano Res.*, 2019, **12**(9), 2288–2295, DOI: **10.1007/s12274-019-2391-y**.

82 Y. Ou, L. P. Twight, B. Samanta, L. Liu, S. Biswas, J. L. Fehrs, N. A. Sagui, J. Villalobos, J. Morales-Santelices, D. Antipin, M. Risch, M. C. Toroker and S. W. Boettcher, Cooperative Fe Sites on Transition Metal (Oxy)Hydroxides Drive High Oxygen Evolution Activity in Base, *Nat. Commun.*, 2023, **14**(1), 7688, DOI: **10.1038/s41467-023-43305-z**.

83 L. Zhang, Q. Xu, Y. Hu, Y. Chen and H. Jiang, Benchmarking the PH-Stability Relationship of Metal Oxide Anodes in Anion Exchange Membrane Water Electrolysis, *ACS Sustainable Chem. Eng.*, 2023, **11**(36), 13251–13259, DOI: **10.1021/acssuschemeng.3c01619**.

84 K. Natarajan, E. Munirathinam and T. C. K. Yang, Operando Investigation of Structural and Chemical Origin of Co3O4 Stability in Acid under Oxygen Evolution Reaction, *ACS Appl. Mater. Interfaces*, 2021, **13**(23), 27140–27148, DOI: **10.1021/acsami.1c07267**.

85 T. M. Chung, S. S. Lee, W. Cho, M. Kim, Y. K. Lee, J. H. Hwang, K. S. An and C. G. Kim, Volatile Nickel Aminoalkoxide Complexes as Liquid Precursors for Non-Volatile Memory Device of NiO Films by ALD, *Bull. Korean Chem. Soc.*, 2011, **32**(3), 783–784, DOI: **10.5012/bkcs.2011.32.3.783**.

86 M. E. Donders, H. C. M. Knoops, W. M. M. Kessels and P. H. L. Notten, Co3O4 as Anode Material for Thin Film Micro-Batteries Prepared by Remote Plasma Atomic Layer Deposition, *J. Power Sources*, 2012, **203**, 72–77, DOI: **10.1016/j.jpowsour.2011.12.020**.

87 D. K. Nandi, J. Manna, A. Dhara, P. Sharma and S. K. Sarkar, Atomic Layer Deposited Cobalt Oxide: An Efficient Catalyst for NaBH4 Hydrolysis, *J. Vac. Sci. Technol., A*, 2016, **34**(1), DOI: **10.1116/1.4935353**.

88 M. E. Donders, H. C. M. Knoops, M. C. M. Van, W. M. M. Kessels and P. H. L. Notten, Remote Plasma Atomic Layer Deposition of Co3O4 Thin Films, *J. Electrochem. Soc.*, 2011, **158**(4), G92, DOI: **10.1149/1.3552616**.

89 V. Miikkulainen, M. Leskelä, M. Ritala and R. L. Puurunen, Crystallinity of Inorganic Films Grown by Atomic Layer Deposition: Overview and General Trends, *J. Appl. Phys.*, 2013, **113**(2), DOI: **10.1063/1.4757907**.

90 R. T. M. van Limpt, M. Lavorenti, M. A. Verheijen, M. N. Tsampas and M. Creatore, Control by Atomic Layer Deposition over the Chemical Composition of Nickel Cobalt Oxide for the Oxygen Evolution Reaction, *J. Vac. Sci. Technol., A*, 2023, **41**(3), 32407, DOI: **10.1116/6.0002414**.

91 A. P. Grosvenor, M. C. Biesinger, R. S. C. Smart and N. S. McIntyre, New Interpretations of XPS Spectra of Nickel Metal and Oxides, *Surf. Sci.*, 2006, **600**(9), 1771–1779, DOI: **10.1016/j.susc.2006.01.041**.

92 M. C. Biesinger, B. P. Payne, L. W. M. Lau, A. Gerson and R. S. C. Smart, X–ray Photoelectron Spectroscopic Chemical State Quantification of Mixed Nickel Metal, Oxide and Hydroxide Systems, *Surf. Interface Anal.*, 2009, **41**(4), 324–332, DOI: **10.1002/sia.3026**.

93 N. S. McIntyre and M. G. Cook, X-Ray, Photoelectron Studies on Some Oxides and Hydroxides of Cobalt, Nickel, and Copper, *Anal. Chem.*, 1975, **47**(13), 2208–2213, DOI: **10.1021/ac60363a034**.

94 D. B. Mitton, J. Walton and G. E. Thompson, An XPS and AES Study of the Ageing of a Co–20%Ni Metal–evaporated Tape, *Surf. Interface Anal.*, 1993, **20**(1), 36–42, DOI: **10.1002/sia.740200107**.

95 M. C. Biesinger, B. P. Payne, A. P. Grosvenor, L. W. M. Lau, A. R. Gerson and R. S. C. Smart, Resolving Surface Chemical States in XPS Analysis of First Row Transition Metals, Oxides and Hydroxides: Cr, Mn, Fe, Co and Ni, *Appl. Surf. Sci.*, 2011, **257**(7), 2717–2730, DOI: **10.1016/j.apsusc.2010.10.051**.

96 D. Cabrera–German, G. Gomez–Sosa and A. Herrera–Gomez, Accurate Peak Fitting and Subsequent Quantitative Composition Analysis of the Spectrum of Co2p Obtained with Al Kα Radiation: I: Cobalt Spinel, *Surf. Interface Anal.*, 2016, **48**(5), 252–256, DOI: **10.1002/sia.5933**.

97 C. V. Thompson and R. Carel, Texture Development in Polycrystalline Thin Films, *Mater. Sci. Eng., B*, 1995, **32**(3), 211–219, DOI: **10.1016/0921-5107(95)03011-5**.

98 D. Cappus, C. Xu, D. Ehrlich, B. Dillmann, C. A. Ventrice, K. Al Shamery, H. Kuhlenbeck and H. J. Freund, Hydroxyl Groups on Oxide Surfaces: NiO(100), NiO(111) and Cr2O3 (111), *Chem. Phys.*, 1993, **177**(2), 533–546, DOI: **10.1016/0301-0104(93)80031-4**.

99 H. B. Profijt, P. Kudlacek, M. C. M. van de Sanden and W. M. M. Kessels, Ion and Photon Surface Interaction during Remote Plasma ALD of Metal Oxides, *J. Electrochem. Soc.*, 2011, **158**(4), G88, DOI: **10.1149/1.3552663**.

100 H. B. Profijt, S. E. Potts, M. C. M. van de Sanden and W. M. M. Kessels, Plasma-Assisted Atomic Layer Deposition: Basics, Opportunities, and Challenges, *J. Vac. Sci. Technol., A*, 2011, **29**(5), DOI: **10.1116/1.3609974**.

101 R. Zhao, S. Xiao, S. Yang and X. Wang, Surface Thermolytic Behavior of Nickel Amidinate and Its Implication on the Atomic Layer Deposition of Nickel Compounds, *Chem. Mater.*, 2019, **31**(14), 5172–5180, DOI: **10.1021/acs.chemmater.9b01267**.

102 D. M. Hercules, Electron Spectroscopy for Chemical Analysis, *Proc. Soc. Anal. Chem.*, 1973, **10**(12), 193–194, DOI: **10.1142/9789811278891_0004**.

103 K. Mukherjee, D. Kreugel, N. Phung, C. van Helvoirt, V. Zardetto and M. Creatore, On the VOC Loss in NiO-Based Inverted Metal Halide Perovskite Solar Cells, *Mater. Adv.*, 2024, **5**(21), 8652–8664, DOI: **10.1039/D4MA00873A**.

104 S. B. S. Heil, E. Langereis, F. Roozeboom, M. C. M. van de Sanden and W. M. M. Kessels, Low-Temperature Deposition of TiN by Plasma-Assisted Atomic Layer Deposition, *J. Electrochem. Soc.*, 2006, **153**(11), G956, DOI: **10.1149/1.2344843**.

105 K. E. K. Holden and J. F. Conley, Characterization of Atomic Layer Deposited Semiconducting Co3O4, *J. Vac. Sci. Technol., A*, 2019, **37**(2), DOI: **10.1116/1.5064469**.

106 J. A. Maxwell, J. L. Campbell and W. J. Teesdale, The Guelph PIXE Software Package, *Nucl. Instrum. Methods Phys. Res., Sect. B*, 1989, **43**(2), 218–230, DOI: **10.1016/0168-583X(89)90042-6**.

107 N. P. Barradas and C. Jeynes, Advanced Physics and Algorithms in the IBA DataFurnace, *Nucl. Instrum. Methods Phys. Res., Sect. B*, 2008, **266**(8), 1875–1879, DOI: **10.1016/j.nimb.2007.10.044**.